Adiabatic optical parametric oscillators: steady-state and dynamical behavior

C. R. Phillips* **and M. M. Fejer**

[1]*E. L. Ginzton Laboratory, Stanford University, 348 Via Pueblo Mall, Stanford California 94305, USA*

**chris.phillips@stanford.edu*

Abstract: We study singly-resonant optical parametric oscillators with chirped quasi-phasematching gratings as the gain medium, for which adiabatic optical parametric amplification has the potential to enhance conversion efficiency. This configuration, however, has a modulation instability which must be suppressed in order to yield narrowband output signal pulses. We show that high conversion efficiency can be achieved by using either a narrowband seed or a high-finesse intracavity etalon.

OCIS codes: (190.4970) Parametric oscillators and amplifiers; (190.3100) Instabilities and chaos; (190.4410) Nonlinear optics, parametric processes; (190.4360) Nonlinear optics, devices; ((230.4320) Nonlinear optical devices; (320.7110) Ultrafast nonlinear optics.

References and links

1. H. Suchowski, V. Prabhudesai, D. Oron, A. Arie, and Y. Silberberg, "Robust adiabatic sum frequency conversion," Opt. Express **17**, 12731–12740 (2009).
2. C. R. Phillips and M. M. Fejer, "Efficiency and phase of optical parametric amplification in chirped quasi-phase-matched gratings," Opt. Lett. **35**, 3093–3095 (2010).
3. C. Heese, C. R. Phillips, L. Gallmann, M. M. Fejer, and U. Keller, "Ultrabroadband, highly flexible amplifier for ultrashort midinfrared laser pulses based on aperiodically poled Mg:$LiNbO_3$," Opt. Lett. **35**, 2340–2342 (2010).
4. M. Charbonneau-Lefort, B. Afeyan, and M. M. Fejer, "Optical parametric amplifiers using chirped quasi-phase-matching gratings I: practical design formulas," J. Opt. Soc. Am. B **25**, 463–480 (2008).
5. G. Imeshev, M. M. Fejer, A. Galvanauskas, and D. Harter, "Pulse shaping by difference-frequency mixing with quasi-phase-matching gratings," J. Opt. Soc. Am. B **18**, 534–539 (2001).
6. L. Gallmann, G. Steinmeyer, U. Keller, G. Imeshev, M. M. Fejer, and J. Meyn, "Generation of sub-6-fs blue pulses by frequency doubling with quasi-phase-matching gratings," Opt. Lett. **26**, 614–616 (2001).
7. M. Charbonneau-Lefort, B. Afeyan, and M. M. Fejer, "Competing collinear and noncollinear interactions in chirped quasi-phase-matched optical parametric amplifiers," J. Opt. Soc. Am. B **25**, 1402–1413 (2008).
8. M. Charbonneau-Lefort, M. M. Fejer, and B. Afeyan, "Tandem chirped quasi-phase-matching grating optical parametric amplifier design for simultaneous group delay and gain control," Opt. Lett. **30**, 634–636 (2005).
9. K. A. Tillman and D. T. Reid, "Monolithic optical parametric oscillator using chirped quasi-phase matching," Opt. Lett. **32**, 1548–1550 (2007).
10. K. A. Tillman, D. T. Reid, D. Artigas, J. Hellstrm, V. Pasiskevicius, and F. Laurell, "Low-threshold femtosecond optical parametric oscillator based on chirped-pulse frequency conversion," Opt. Lett. **28**, 543–545 (2003).
11. J. A. Armstrong, N. Bloembergen, J. Ducuing, and P. S. Pershan, "Interactions between light waves in a nonlinear dielectric," Phys. Rev. **127**, 1918–1939 (1962).
12. W. R. Bosenberg, A. Drobshoff, J. I. Alexander, L. E. Myers, and R. L. Byer, "93% pump depletion, 3.5-w continuous-wave, singly resonant optical parametric oscillator," Opt. Lett. **21**, 1336–1338 (1996).
13. C. R. Phillips and M. M. Fejer, "Stability of the singly resonant optical parametric oscillator," J. Opt. Soc. Am. B **27**, 2687–2699 (2010).
14. C. R. Phillips, J. S. Pelc, and M. M. Fejer, "Continuous wave monolithic quasi-phase-matched optical parametric oscillator in periodically poled lithium niobate," Opt. Lett. **36**, 2973–2975 (2011).
15. S. T. Yang, R. C. Eckardt, and R. L. Byer, "Power and spectral characteristics of continuous-wave parametric oscillators: the doubly to singly resonant transition," J. Opt. Soc. Am. B **10**, 1684–1695 (1993).

#158303 - $15.00 USD Received 16 Nov 2011; revised 23 Dec 2011; accepted 27 Dec 2011; published 19 Jan 2012

16. L. E. Myers and W. R. Bosenberg, "Periodically poled lithium niobate and quasi-phase-matched optical parametric oscillators," IEEE J. Quantum. Electron. **33**, 1663–1672 (1997).
17. A. Henderson and R. Stafford, "Spectral broadening and stimulated Raman conversion in a continuous-wave optical parametric oscillator," Opt. Lett. **32**, 1281–1283 (2007).
18. J. Kiessling, R. Sowade, I. Breunig, K. Buse, and V. Dierolf, "Cascaded optical parametric oscillations generating tunable terahertz waves in periodically poled lithium niobate crystals," Opt. Express **17**, 87–91 (2009).
19. R. Sowade, I. Breunig, I. Cmara Mayorga, J. Kiessling, C. Tulea, V. Dierolf, and K. Buse, "Continuous-wave optical parametric terahertz source," Opt. Express **17**, 22303–22310 (2009).
20. A. V. Smith, R. J. Gehr, and M. S. Bowers, "Numerical models of broad-bandwidth nanosecond optical parametric oscillators," J. Opt. Soc. Am. B **16**, 609–619 (1999).
21. A. V. Smith, "Bandwidth and group-velocity effects in nanosecond optical parametric amplifiers and oscillators," J. Opt. Soc. Am. B **22**, 1953–1965 (2005).
22. G. Arisholm, "Quantum noise initiation and macroscopic fluctuations in optical parametric oscillators," J. Opt. Soc. Am. B **16**, 117–127 (1999).
23. G. Arisholm, "General analysis of group velocity effects in collinear optical parametric amplifiers and generators," Opt. Express **15**, 6513–6527 (2007).
24. G. Arisholm, G. Rustad, and K. Stenersen, "Importance of pump-beam group velocity for backconversion in optical parametric oscillators," J. Opt. Soc. Am. B **18**, 1882–1890 (2001).
25. R. White, Y. He, B. Orr, M. Kono, and K. Baldwin, "Transition from single-mode to multimode operation of an injection-seeded pulsed optical parametric oscillator," Opt. Express **12**, 5655–5660 (2004).
26. A. Yariv, *Quantum Electronics*, 3rd ed. (Wiley, 1989).
27. G. Agrawal, *Nonlinear Fiber Optics*, 4th ed. (Academic Press, 2007).
28. C. R. Phillips, C. Langrock, J. S. Pelc, M. M. Fejer, I. Hartl, M. E. Fermann, "Supercontinuum generation in quasi-phasematched waveguides," Opt. Express **19**, 18754–18773 (2011)
29. C. R. Phillips, C. Langrock, J. S. Pelc, M. M. Fejer, J. Jiang, M. E. Fermann, I. Hartl, "Supercontinuum generation in quasi-phasematched $LiNbO_3$ waveguide pumped by a Tm-doped fiber laser system," Opt. Lett. **36**, 3912–3914 (2011)
30. M. Conforti, F. Baronio, and C. De Angelis, "Nonlinear envelope equation for broadband optical pulses in quadratic media," Phys. Rev. A **81**, 053841 (2010).
31. R. A. Baumgartner and R. L. Byer, "Optical parametric amplification," IEEE J. Quantum Electron. **15** (6), 432 (1979)
32. Crisp, M. D, "Adiabatic-following approximation," Phys. Rev. A **8**, 2128–2135 (1973).
33. G. Luther, M. Alber, J. Marsden, and J. Robbins, "Geometric analysis of optical frequency conversion and its control in quadratic nonlinear media," J. Opt. Soc. Am. B **17**, 932–941 (2000).
34. O. Gayer, Z. Sacks, E. Galun, and A. Arie, "Temperature and wavelength dependent refractive index equations for MgO-doped congruent and stoichiometric $LiNbO_3$," Appl. Phys. B: Lasers and Optics **91**, 343–348 (2008).
35. K. L. Vodopyanov "Optical THz-wave generation with periodically-inverted GaAs" Laser Photon. Rev. **2**, No. 1-2, 11–25 (2008)
36. G.-L. Oppo, M. Brambilla, and L. A. Lugiato, "Formation and evolution of roll patterns in optical parametric oscillators," Phys. Rev. A **49**, 2028–2032 (1994)
37. J. E. Schaar, "Terahertz Sources Based On Intracavity Parametric Frequency Down-Conversion Using Quasi-Phase-Matched Gallium Arsenide," Ph.D. thesis, Stanford University (2009)
38. M. J. Lawrence, B. Willke, M. E. Husman, E. K. Gustafson, and R. L. Byer, "Dynamic response of a Fabry-Perot interferometer," J. Opt. Soc. Am. B **16**, 523–532 (1999).

1. Introduction

Chirped (aperiodic) quasi-phasematching (QPM) gratings have received attention for many optical frequency conversion schemes including difference frequency generation (DFG), optical parametric amplification (OPA), sum frequency generation (SFG), and related applications [1–10]. Their main role so far has been to broaden the phasematching bandwidth compared to conventional periodic QPM gratings, without the need to use short crystals with reduced conversion efficiency. This broadening can be understood through a simple spatial frequency argument: due to dispersion, there is a mapping between phasematched frequency and grating k-vector; in chirped QPM gratings, the grating k-vector is swept smoothly over the range of interest, thereby broadening the spatial Fourier spectrum of the grating and hence the phasematching bandwidth [1, 5–7].

More recently it has been shown that nonlinear interactions in chirped QPM gratings can exhibit high efficiencies due to an adiabatic following process [1, 2]. For three-wave mixing

#158303 - $15.00 USD Received 16 Nov 2011; revised 23 Dec 2011; accepted 27 Dec 2011; published 19 Jan 2012

processes involving input pump and signal waves and a generated idler wave, the ratio of pump output and input intensities asymptotes to 0 with respect to both the input signal and pump intensities, i.e. asymptotes to 100% pump depletion. This behavior occurs for interactions that are both plane-wave and monochromatic, provided that the QPM grating is sufficiently chirped. For non-diffracting (near-field) beams, all transverse spatial components interact independently and as plane waves. Thus, for interactions involving non-diffracting beams, all spatial components of the pump beam can asymptote to 100% depletion with respect to the pump and signal powers.

For conventional interactions involving birefringent phasematching or periodic QPM gratings, there is a mapping between signal and pump intensity and the propagation distance required to fully deplete the pump, defined as L_{NL}; after L_{NL}, back-conversion occurs, transferring energy back to the pump from the signal and idler waves [11]. As a result, complete conversion across the spatial profile of non-diffracting Gaussian beams cannot usually be achieved. Back-conversion can also limit the conversion efficiency even for plane-wave interactions involving pulses with bandwidths narrow enough that group velocity mismatch (GVM) and group velocity dispersion (GVD) effects are negligible, since in this case all temporal components interact independently in a single pass through the nonlinear crystal. In the spatial domain, the conversion efficiency can be enhanced by using near-confocal focusing [12]; in the time domain, the conversion efficiency can be enhanced by using pulses with durations short enough that GVM is non-negligible. For wide (non-diffracting) beams, beam shaping (e.g. flat-top beam profiles) is required in order to yield an L_{NL} that is independent of transverse spatial position. The use of chirped QPM gratings offers a way of removing the above limitations on conversion efficiency of pulsed beams (in both the spatial and temporal domains) without the need for small beam areas, short pulse durations, or beam shaping.

One example where this efficiency enhancement could be useful is in nanosecond optical parametric oscillators (OPOs). Optical parametric oscillators have been studied extensively in many regimes including for continuous wave (CW) pumping [12–19], and for ns pump pulses [20–25]. Chirped QPM gratings have been used as the gain medium in OPOs [9, 10], but their properties have not yet been fully explored in the context of adiabatic conversion. In order to reach the high conversion efficiencies predicted by the plane-wave CW theory (which we discuss in Section 3 and generate clean output pulses, the OPO signal wave must also be modulationally stable against noise, so that upon successive trips around the optical cavity it converges to a pulsed beam with a near-transform-limited spatiotemporal profile. It has been shown that OPOs using periodic QPM gratings or birefringent phasematching exhibit a temporal modulation instability (MI) [13]. In this paper, we show that chirped QPM OPOs are even more susceptible to modulationally instabilities, discuss the suppression of the MI with additional intracavity elements, and numerically simulate the dynamics of chirped QPM ns-pumped OPOs.

2. Coupled wave equations

In this section, we introduce coupled-wave equations suitable for analyzing the steady-state, modulation instability, and nonlinear dynamics of OPOs. The equations we use are quite general, allowing for arbitrary QPM grating profiles and including an additional backwards THz wave which, in recent work [14, 18, 19], has been shown to influence OPO behavior (though the MI can exist without the THz interaction). The coupled wave equations we use are similar to other formulations of pulse propagation in $\chi^{(2)}$ media [13,26,27], and can be derived from more general forward-wave propagation equations [28, 29]. The MI analysis we perform follows that of Ref. [13] quite closely, but here we will consider OPOs using chirped QPM gratings as the gain medium.

#158303 - $15.00 USD Received 16 Nov 2011; revised 23 Dec 2011; accepted 27 Dec 2011; published 19 Jan 2012

The coupling between pump, signal, idler and DC envelopes due to the first Fourier order of the QPM grating is given by the following frequency-domain equations,

$$\begin{aligned}
\hat{L}_i\tilde{A}_i &= -i\gamma_{\mathrm{opt}}(\omega)\mathscr{F}\left[A_s^*A_p\right] - i\gamma_{\mathrm{THz}}(\omega)\mathscr{F}\left[(A_T+A_T^*)A_i\right] \\
\hat{L}_s\tilde{A}_s &= -i\gamma_{\mathrm{opt}}(\omega)\mathscr{F}\left[A_i^*A_p\right] - i\gamma_{\mathrm{THz}}(\omega)\mathscr{F}\left[(A_T+A_T^*)A_s\right] \\
\hat{L}_p\tilde{A}_p &= -i\gamma_{\mathrm{opt}}(\omega)\mathscr{F}\left[A_iA_s\right] - i\gamma_{\mathrm{THz}}(\omega)\mathscr{F}\left[(A_T+A_T^*)A_p\right] \\
\hat{L}_T\tilde{A}_T &= -i\gamma_{\mathrm{THz}}(\omega)\mathscr{F}\left[|A_i|^2+|A_s|^2+|A_p|^2\right]
\end{aligned} \tag{1}$$

where $\mathscr{F}$ denotes the Fourier transform, and where ω represents optical frequency (as opposed to a Fourier transform variable centered at one of the carrier frequencies ω_j). Subscripts i, s, p and T represent quantities associated with the idler, signal, pump and DC envelopes; we use subscript "T" because including the DC envelope (centered at zero frequency) leads to phase-matched THz-frequency interactions. Tilde denotes an envelope represented in the frequency domain. The envelopes A_j are analytic signals ($\tilde{A}_j(\omega)=0$ for $\omega<0$), and are assumed to have non-overlapping spectra; the use of analytic signals is appropriate in general [28, 30], and is especially useful for modeling interactions involving A_T. With these constraints, the envelopes are fully specified via the real-valued electric field which is related to the envelopes by

$$\begin{aligned}
E = &\frac{1}{2}\left[\left(A_ie^{i(\omega_it-k_iz)}+A_se^{i(\omega_st-k_sz)}+A_pe^{i(\omega_pt-k_pz)}\right)e^{-i\int_0^z\Delta k(z')dz'}+A_Te^{(-i\int_0^zK_g(z')dz')}\right] \\
&+\text{c.c.},
\end{aligned} \tag{2}$$

where c.c denotes complex conjugate. The carrier frequencies are ω_j. The wavevector is given by $k(\omega)$, and carrier propagation coefficients are given by $k_j\equiv k(\omega_j)$. The QPM grating k-vector is given by $K_g(z)$. We define the material phase mismatch as $\Delta k_0 = k_p - k_s - k_i$, and the carrier phase mismatch as

$$\Delta k(z) = \Delta k_0 - K_g(z). \tag{3}$$

The linear propagation operators in Eq. (1) are given for the pump, signal and idler by

$$\hat{L}_j = \frac{\partial}{\partial z} + \frac{\alpha(\omega)}{2} + i\left[k(\omega) - \frac{k_x^2+k_y^2}{2k(\omega)} - k_j - \frac{\omega-\omega_j}{v_{\mathrm{ref}}}\right] - i\Delta k(z) \tag{4}$$

for spatial frequencies k_x and k_y, and reference velocity v_{ref}, which we choose to be the group velocity at ω_s. The form of $\hat{L}_j$ in Eq. (4) assumes paraxial diffraction in an isotropic medium. For propagation normal to the optical axis of an anisotropic medium, minor modifications are required for L_j, but these do not significantly change the results of this analysis. For propagation at finite angles to the optical axis, first-order terms in k_x or k_y will appear and substantially alter the results; this case is beyond the scope of this paper. The linear propagation operator for the DC envelope, $\hat{L}_T$, has a similar form to $\hat{L}_j$, modified for a backwards-propagating wave,

$$\hat{L}_T = \frac{\partial}{\partial z} - \frac{\alpha(\omega)}{2} - i\left[k(\omega) - \frac{k_x^2+k_y^2}{2k(\omega)} + \frac{\omega}{v_{\mathrm{ref}}} - K_g(z)\right] \tag{5}$$

where $\alpha(\omega)$ is the frequency-dependent power attenuation coefficient. We will neglect $\alpha(\omega)$ at optical frequencies but not at THz frequencies. Finally, the coupling coefficients are given by $\gamma_{\mathrm{opt}}(\omega) = (\omega/c)^2(2d_{\mathrm{opt}})/(\pi k(\omega))$ and $\gamma_{\mathrm{THz}}(\omega) = (\omega/c)^2(2d_{\mathrm{THz}})/(\pi k(\omega))$, where d_{opt} and d_{THz} are the second-order nonlinear coefficients for the optical-optical and optical-THz mixing

#158303 - $15.00 USD Received 16 Nov 2011; revised 23 Dec 2011; accepted 27 Dec 2011; published 19 Jan 2012

processes, respectively, and are determined by the relevant tensor elements and QPM orders. We assume that $d_{\rm opt}$ and $d_{\rm THz}$ are non-dispersive over the frequency ranges of interest.

Equation (1) may be used to evaluate the single-pass propagation for arbitrary OPO configurations. With suitable cavity wrapping [20], Eq. (1) can be used to evaluate OPO dynamics with, for example, semi-classical noise seeding, as we discuss in Section 5.

3. Steady-state solution for chirped QPM OPOs

In this section, we determine the nominal steady-state operating point for CW-pumped, plane-wave, singly-resonant OPOs when using a chirped QPM grating as the gain medium. The condition for the steady state is that the gain should equal the total cavity losses for the resonant signal wave. We define envelopes $A_j^{(0)}(z)$ as the steady-state, z-dependent field profiles found by solving Eq. (1) and imposing self-consistency after a cavity round-trip. These steady-state solutions are greatly simplified by using the asymptotic expressions for the chirped-QPM signal gain and pump depletion which apply for sufficiently strongly chirped QPM profiles [1, 2, 4]. For such QPM profiles, the signal power gain in the undepleted-pump limit is given, approximately, by [4]

$$G_s \approx \exp(2\pi\Lambda_p), \tag{6}$$

where the signal gain coefficient is given by $\Lambda_p = \gamma_{\rm opt}(\omega_i)\gamma_{\rm opt}(\omega_s)|A_p^{(0)}(0)|^2/|\Delta k'|$, and where $\Delta k' = \partial\Delta k/\partial z$ is the QPM chirp rate (units of m^{-2}), assumed to be constant near $\Delta k(z) \approx 0$. To understand this relation, we introduce a peak gain rate $g_0 = [\gamma_{\rm opt}(\omega_i)\gamma_{\rm opt}(\omega_s)]^{1/2}|A_p^{(0)}(0)|$. The local OPA (power) gain rate is then given in terms of the local phase mismatch by $g(z) = 2[g_0^2 - (\Delta k(z)/2)^2]^{1/2}$. This relation is identical to conventional relations for plane-wave interactions in unchirped devices at each point z [31], but is z-dependent here due to the QPM chirp. To find the total gain, this gain rate is integrated over the region for which $\mathrm{Re}[g] > 0$ (i.e. the region of the grating for which the phase mismatch is small enough to allow OPA). For a linear chirp rate, this integration yields Eq. (6); this procedure can be made more formal via WKB analysis [4]. From Eq. (6), the OPO threshold condition is given by $\Lambda_{p,th} = \ln(R_s^{-1})/(2\pi)$, where $\Lambda_{p,th}$ is the threshold signal gain coefficient and $R_s \equiv 1 - a_s$ is the effective net round-trip reflectance (defined in terms of the round-trip signal power loss, a_s).

Above threshold and assuming low cavity losses so that $A_s^{(0)}(z) \approx A_s^{(0)}(0)$, the pump depletion is given, approximately, by [1]

$$\eta_p \approx \exp(-2\pi\Lambda_s), \tag{7}$$

where the pump depletion coefficient is given by $\Lambda_s = \gamma_{\rm opt}(\omega_i)\gamma_{\rm opt}(\omega_p)|A_s^{(0)}(0)|^2/|\Delta k'|$. The pump depletion is defined as $\eta_p = |A_p(L)/A_p(0)|^2$. Again assuming low losses, Eq. (6) and (7) can be used to express the OPO operating point, by equating the decrement to the number of signal photons lost due to the round trip losses and the increment from the depletion of the pump, yielding an implicit equation for the pump depletion coefficient Λ_s,

$$\frac{1-\exp(-2\pi\Lambda_s)}{2\pi\Lambda_s} = \frac{1}{N} \tag{8}$$

where the pump ratio N is the ratio of pump intensity to threshold pump intensity (i.e. the number of times above oscillation threshold). Based on this equation, the circulating signal intensity (which is proportional to Λ_s by definition), and hence the conversion efficiency, are predicted to increase monotonically with pump intensity. This behavior is illustrated in Fig. 1, which shows the pump depletion predicted by solving Eq. (8) for Λ_s as a function of N. Since

#158303 - $15.00 USD Received 16 Nov 2011; revised 23 Dec 2011; accepted 27 Dec 2011; published 19 Jan 2012

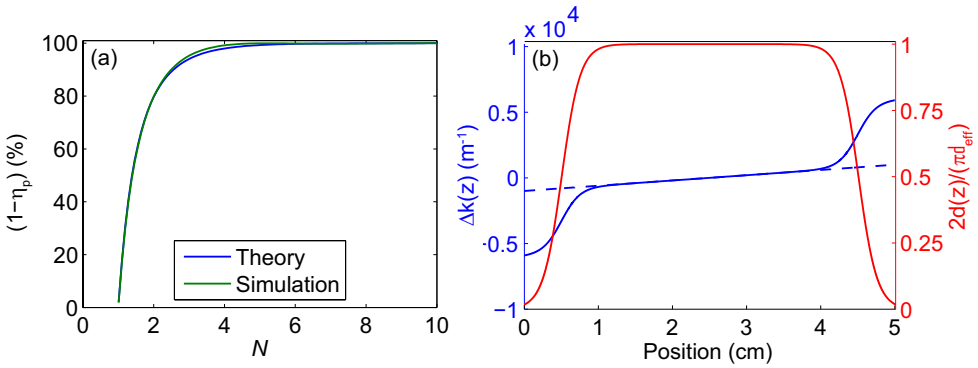

Fig. 1. (a) Conversion efficiency $(1-\eta_p)$ as a function of pump ratio N, for the QPM grating profile shown by the solid blue and red lines in (b); the simulation parameters are given in the text. The dashed straight line in (b) shows just the linear part of the Δk profile (slope $\Delta k'$) as a guide to the eye. The analytical result from Eqs. (7) and (8), labeled "theory" in (a) is in good agreement with the numerical solution of Eq. (1), labeled "simulation" in (a).

conversion efficiency increases monotonically with signal and pump power in regimes with high gain and high pump depletion [2], Eq. (8) qualitatively describes the steady-state OPO behavior even in the presence of moderate signal losses.

To test the validity of Eq. (8), Fig. 1(a) also shows the pump depletion predicted from direct simulations of Eq. (1) using a Runge-Kutta method, assuming plane-wave and CW pump, signal and idler carrier waves; the two are in good agreement, indicating that adiabatic conversion applies very well to CW OPOs. The QPM profile used for the simulation is shown in Fig. 1(b) along with the profile of the nonlinear coefficient $d_{\text{eff}}(z)$ (normalized to its maximum value at a 50% QPM duty cycle); the reduction in $d_{\text{eff}}(z)$ and increase in the chirp rate of $\Delta k(z)$ at the edges of the grating are for apodization [4], which is necessary to reach the high efficiencies predicted by Eq. (8). The functional form of the QPM profile is given by

$$K_g(z) = k_p - k_s - k_i - \Delta k'(z - L/2) - \frac{K_a}{2}\left[\tanh\left(\frac{z-z_{a1}}{L_{a1}}\right) - \tanh\left(\frac{z_{a2}-z}{L_{a2}}\right)\right], \qquad (9)$$

which corresponds to a nominally linear chirp rate $\Delta k'$, with an increase in $|\Delta k(z)|$ near the edges of the grating. The functional form of $d_{\text{eff}}(z)$ is also given by hyperbolic tangent functions. The grating length is L, and $z = 0$ denotes the start of the grating. The chirp rate $\Delta k'$ was chosen such that $|\Delta k' L^2|^{1/2} = 10$ for length L. This choice smoothly sweeps the carrier phase mismatch $\Delta k(z)$ through zero and is sufficient to reveal the important steady-state and MI-related effects that must be considered in the design of any low-cavity-loss OPO using chirped QPM gratings. The parameters K_a, z_{a1}, z_{a2}, L_{a1}, and L_{a2} in Eq. (9) are chosen to smoothly turn the idler on and the pump off at the input and output of the QPM grating, respectively; the quality of this apodization is manifested in a smooth OPA gain spectrum, with low ripple amplitude [4]. For Fig. 1(b), the parameters were $L = 5$ cm, $\Delta k'$=4 cm^{-2}, $K_a = 50$ cm^{-1}, $z_{a1} = 0.1L$, $z_{a2} = 0.9L$, $L_{a1} = 0.05L$, and $L_{a2} = 0.05L$.

In Fig. 2, we show the steady-state spatial profiles of the fields in an OPO with the QPM grating given in Fig. 1(b), by plotting the intensities $I_j(z)$ for the three waves $[j = (i,s,p)]$, normalized to the input pump intensity I_0; for this example, we assume $N = 6$ and $R_s = 95\%$. The pump is converted primarily near the center of the QPM grating, where phasematching is satisfied. Each of the fields is almost $\pi/2$ out of phase with its nonlinear source term throughout the grating (as opposed to in phase in the case of phasematched interactions in periodic QPM

#158303 - $15.00 USD Received 16 Nov 2011; revised 23 Dec 2011; accepted 27 Dec 2011; published 19 Jan 2012

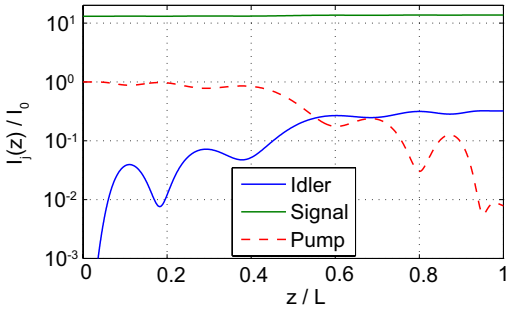

Fig. 2. Steady-state intensity profiles $I_j(z)$ normalized to input pump intensity I_0 for the OPO simulated in Fig. 1, for $N = 6$.

gratings), corresponding to adiabatic following of local nonlinear eigenmodes [32, 33].

Based on Fig. 1(a), it is possible to significantly exceed the conversion efficiency that can be obtained with Gaussian beams in periodic QPM gratings or birefringently phasematched media, without performing any beam shaping, provided that one operates far enough above oscillation threshold. In the limit of long pulses and large beams, the condition for high conversion efficiency is that $N(x,y) \gg 1$ across most of the spatiotemporal profile of the pump (positions x and y). By using a signal cavity mode somewhat larger than the pump beam and a cavity lifetime comparable to or longer than the duration of the pump pulse, this condition is more easily attained.

4. Temporal MI for chirped QPM OPO

In order to achieve the high conversion efficiency predicted by Fig. 1(a), the OPO steady-state solution must be stable against the quantum noise present at all frequencies. In this section, we will show that for any pump ratio $N > 1$, chirped QPM OPOs exhibit a temporal modulation instability. In order to yield a single-mode or narrow-band signal, this MI must be suppressed (by an intracavity etalon, for example).

A general formalism for analyzing the OPO MI is given in Appendix (A), similar to the approach detailed in Ref. [13]. To calculate the MI gain, we find the z-dependent steady-state solutions of Eq. (1), and then use Eq. (1) to calculate the single-pass amplification of small sidebands, detuned from the respective carrier frequencies by an amount $\pm\Omega$, superposed on each of the envelopes. We assume that Ω is positive (without loss of generality), so these sidebands have absolute optical frequencies $\omega = \omega_j \pm \Omega$ (for $j = i, s, p$, corresponding to the idler, signal, and pump envelopes) and $\omega = \Omega$ (corresponding to the DC envelope, A_T). While the formalism we develop can address the general case of non-collinear sidebands, in this section, we use that formalism to evaluate the MI of chirped QPM, plane-wave OPOs with collinear sidebands, i.e. for sideband spatial frequency $k_x = k_y = 0$. For simplicity we consider the profile given by Eq. (9). Different grating profiles will exhibit comparable behavior provided that the phase mismatch is swept smoothly, monotonically, and slowly through zero, and has sufficiently large magnitude at $z = 0$ and $z = L$.

Figure 3(a) shows the frequency dependence of the net sideband gain (assuming out-coupling and cavity losses totaling 5%) associated with the steady state solutions. For the simulation, we chose $\lambda_p = 1.064$ μm, $\lambda_s = 1.55$ μm, and the temperature $T = 150^\circ$ C, and use the nonlinear coefficients and dispersion relation of MgO:$LiNbO_3$ [34, 35]. For any given pump ratio N, there is a range of frequencies for which there is MI gain ($G > 0$). Therefore, this OPO would not

#158303 - $15.00 USD Received 16 Nov 2011; revised 23 Dec 2011; accepted 27 Dec 2011; published 19 Jan 2012

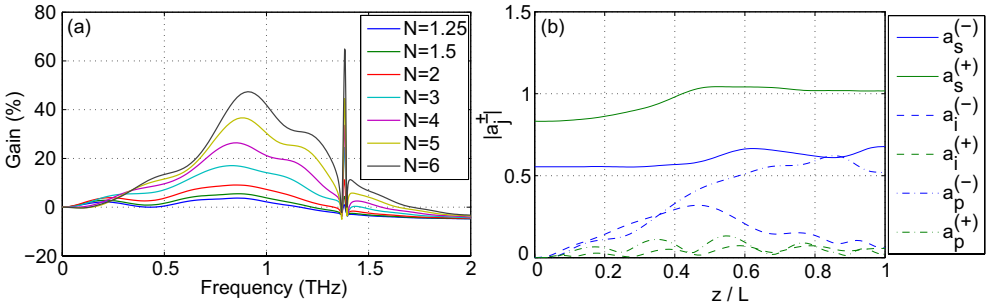

Fig. 3. (a) Dependence of sideband gain G on pump ratio N for the OPO simulated in Fig. 1. (b) Propagation of the signal, idler and pump sidebands for the highest-gain signal eigenmode at $\Omega/(2\pi) = 1$ THz and $N = 6$. The sidebands are normalized such that $|a_s^-|^2 + |a_s^+|^2 = 1$ at $z = 0$.

operate in a single mode. The MI is not an artifact of the particular parameters used for Fig. 3(a), but occurs for many resonant wavelengths and chirp rates, provided that there is a sufficient grating chirp for adiabatic conversion to occur. However, the structure of the net sideband gain does depend on the material dispersion, as with conventional OPOs [13].

In Fig. 3(a), the peak around 1.38 THz is related to the strongly-absorbed backwards THz wave. At this frequency, the interaction between the $A_s^{(0)}$, $a_s^{(-)}$, and $a_T^{(+)}$ waves is phasematched, leading to optical parametric amplification at the Stokes-frequency-shifted signal sideband $a_s^{(-)}$; we denote this process as THz-OPA. In the limit of a large THz absorption α_T, the THz-OPA gain is inversely proportional to α_T [14], and the THz-OPA process is similar to stimulated Raman scattering. Since α_T is large in $LiNbO_3$ at 1.38 THz [35], the THz peak in Fig. 3(a) is damped substantially compared to predictions if absorption was neglected. However, despite this damping, the signal sideband gain still exceeds the cavity losses. For materials with a higher THz absorption, the strength of the THz-OPA peak compared to the other features seen in Fig. 3(a) would be reduced.

Away from 1.38 THz, the THz-OPA process is highly phase mismatched and can be neglected. As a result, in most spectral regions, the MI corresponds to the pump, signal and idler three-wave mixing process [13]. This process is illustrated in Fig. 3(b), which shows the propagation of sidebands through the QPM grating (sidebands detuned from carrier frequencies by ± 1 THz). The generation and amplification of these sidebands can be understood through phasematching arguments: the phase mismatch for an interaction between a pair of sidebands and a carrier wave can be defined as the phase accumulated by one of those sidebands relative to the phase of its driving polarization, assuming that the sidebands were to propagate linearly (i.e. with phases unperturbed by $\chi^{(2)}$). Consider the interaction between an idler sideband $\tilde{a}_i(\mp\Omega)$, a signal sideband $\tilde{a}_s(\pm\Omega)$, and the pump wave carrier $A_p^{(0)}$. Based on the above assumption, the phase mismatch for this process is given by

$$\Delta k_{is,\mathrm{eff}}(z,\pm\Omega) \approx \Delta k(z) - \frac{\partial \phi_p}{\partial z} \pm \left(\frac{n_{g,i} - n_{g,s}}{c}\right)\Omega, \tag{10}$$

where $n_{g,j}$ is the group index of wave j, and ϕ_j is the phase of carrier wave $A_j^{(0)}(z)$; higher orders of dispersion have been neglected for simplicity. The carrier phase mismatch $\Delta k(z)$ is given by Eq. (3). Similarly, for the interaction between a signal sideband $\tilde{a}_s(\pm\Omega)$, a pump

#158303 - $15.00 USD Received 16 Nov 2011; revised 23 Dec 2011; accepted 27 Dec 2011; published 19 Jan 2012

sideband $\tilde{a}_p(\pm\Omega)$, and the idler carrier wave $A_i^{(0)}$, the phase mismatch is given by

$$\Delta k_{sp,\mathrm{eff}}(z,\pm\Omega) \approx \Delta k(z) + \frac{\partial \phi_i}{\partial z} \pm \left(\frac{n_{g,p} - n_{g,s}}{c}\right)\Omega. \tag{11}$$

Lastly, for an interaction between an idler sideband $\tilde{a}_i(\pm\Omega)$, a pump sideband $\tilde{a}_p(\pm\Omega)$, and the signal carrier wave $A_s^{(0)}$, the phase mismatch is given by

$$\Delta k_{ip,\mathrm{eff}}(z,\pm\Omega) \approx \Delta k(z) + \frac{\partial \phi_s}{\partial z} \pm \left(\frac{n_{g,p} - n_{g,i}}{c}\right)\Omega. \tag{12}$$

For the example in Fig. 3(b), the sideband frequency is 1 THz, and the group indices for the idler, signal and pump waves are given 2.2081, 2.1795, and 2.2091, respectively. The carrier wave phase accumulation can often be neglected, since the steady-state fields only accumulate phase rapidly when the field amplitude is low compared to the other two waves; such fields do not contribute strongly to the sideband generation process. The apodization regions can also be neglected for simplicity, since only weak sideband generation can occur there due to the high chirp rate. With these assumptions, for the interaction between signal and idler sidebands, $\Delta k_{is,\mathrm{eff}}(z,+\Omega) = 0$ at $z = z_{pm,is}(+\Omega) \approx -0.3L$, where the pump is undepleted [see Fig (2)]. For the interaction between idler and pump sidebands, $\Delta k_{ip,\mathrm{eff}}(z,\pm\Omega) = 0$ at $z = z_{pm,ip}(\pm\Omega) \approx \mp 0.01L$, which involves the strong steady-state signal field. For the interaction between signal and pump sidebands, $\Delta k_{sp,\mathrm{eff}}(z,-\Omega) = 0$ at $z = z_{pm,sp}(-\Omega) \approx 0.31L$; this interaction involves the steady-state idler field, which is strong at $z_{pm,sp}(-\Omega)$.

The above considerations explain why the signal sidebands can experience gain greatly in excess of the signal carrier wave: at most points in the QPM grating, one of the pairs of sidebands is close to phasematching and is driven strongly by the corresponding steady-state field; the sidebands can thus arrange themselves for strong sideband amplification and generation over much of the grating due to the existence of multiple phasematched points for the various sideband mixing processes; this amplification can be seen in Fig. 3(b). These processes are in contrast to the interaction between the carrier waves, in which the signal is amplified only in the vicinity of the single phasematched point where $\Delta k(z) = 0$ (and in which each of the waves is nearly $\pi/2$ out of phase with its nonlinear source term due to the adiabatic following process).

The type of behavior discussed in this section, where the QPM chirp reduces the gain for the CW signal wave compared to a parasitic process (in this case, sideband amplification), has also been seen in the spatial domain when using finite-sized beams [3, 7]. In general, it may also be necessary to consider additional nonlinear processes such as stimulated Raman scattering (SRS) for which amplification occurs over the entire length of the QPM grating; SRS would be relevant in cases where the cavity losses are low at any Stokes-shifted wavelengths. Additional waves and nonlinear effects can be added relatively straightforwardly to Eq. (21) [28].

In order to build an OPO with narrow-band, low-noise output signal pulses, the modulation instability must be adequately suppressed. One way to suppress the MI is by introducing an intracavity element such as an etalon to create loss selectively at the sideband frequencies, such that $G(\Omega) < 1$ for all sideband frequency detunings Ω. Thus, if an etalon is used, the free spectral range should be comparable to the MI gain bandwidth [as shown in Fig. 3(a) for a particular example], and the finesse must introduce sufficient loss at sideband frequencies within this spectral region that $G(\Omega) < 1$. The required etalon facet reflectance R to fully suppress the MI can be estimated as $[(1-R)/(1+R)]^2 = (G_0)^{-1}$, where G_0 denotes the peak MI gain in the absence of the etalon. In cases where the design parameters of a single intracavity etalon would be too constrained, multiple etalons or the combination of an etalon and a diffraction grating could be used.

#158303 - $15.00 USD Received 16 Nov 2011; revised 23 Dec 2011; accepted 27 Dec 2011; published 19 Jan 2012

For a CW OPO, $G < 1$ is necessary to avoid sideband amplification in the steady-state. Based on Fig. 3(a), a high reflectance etalon (e.g. with $R > 75\%$) is needed. This reflectance is significantly higher than that required to yield stable operation of CW-pumped OPOs using periodic QPM gratings, for which Fresnel reflections from uncoated optics are sufficient [13]. For nanosecond pump pulses, the sidebands are amplified or suppressed over several cavity round-trips (corresponding to the duration of the pump), and hence the signal spectrum will continue to narrow as G is reduced. Conversely, it may not be necessary to fully suppress the MI within the etalon peak corresponding to the signal carrier frequency in order to achieve adiabatic conversion. The design issues associated with nanosecond-pumped chirped QPM OPOs are discussed in Section 5.

5. Numerical simulation of chirped QPM OPOs

The OPO efficiency enhancements made possible by chirped QPM gratings are likely to be most advantageous when using a pulsed pump, since high efficiencies are already possible for CW-pumped OPOs by appropriate near-confocal resonator design [12]. The OPO configuration where Eq. (8) can apply most directly is for nanosecond pump pulses, for which dynamical effects including group velocity mismatch and dispersion (GVM and GVD) can, in the ideal limit, be neglected. However, to determine if this narrow-bandwidth limit applies, GVM- and GVD-related effects must be modeled using Eq. (1), together with an appropriate cavity-wrapping procedure [21]. In this section, we perform numerical simulations of a ns-pulse plane-wave OPO with and without an intracavity etalon, in order to see the role that the MI plays when using nanosecond pump pulses.

5.1. Design considerations

When using nanosecond pulses, a number of design constraints must be met, which we outline here. First, the signal must build up from quantum noise to have comparable power to the pump in a reasonably small fraction of the pump duration (since the pump remains undepleted, and hence the operation is inefficient, before signal build-up). To quantify this constraint, we first define the round-trip number as the ratio of pump duration to the cavity round-trip time, $N_{rt} = \tau_p / t_{rt}$. For large N_{rt}, the time-dependent signal intensity during the build-up stage can be expressed approximately as

$$\ln\left(\frac{I(t)}{I_0}\right) \approx N_{rt} \int_{t_0}^{t} \frac{2\pi\Lambda_{p,pk} f_p(t') - \ln(1/R_s)}{\tau_p} dt', \tag{13}$$

where the $2\pi\Lambda_{p,pk}$ is the signal gain coefficient associated with the peak of the pump pulse, and $f_p(t)$ is the pump intensity profile normalized to its peak value, and takes values between 0 and 1. t_0 is the time at which gain exceeds the cavity loss (i.e. where the integrand crosses zero), and I_0 is an effective input noise intensity. The $2\pi\Lambda_{p,pk}$ factor originates from Eq. (6). A second OPO constraint is that the signal should have a cavity lifetime comparable to the pump duration, in order to ensure depletion of the trailing edge of the pump. This constraint is described in terms of N_s, the ratio of pump duration to the signal-cavity lifetime, given by

$$N_s \equiv \ln(1/R_s) N_{rt}. \tag{14}$$

In general N_s should be of order unity. A third OPO constraint is that the pump should be intense enough to support adiabatic conversion on its leading edge, based on Eq. (8), and hence N_{pk}, the ratio of the signal gain at the peak of the pump pulse to the round trip cavity losses,

#158303 - $15.00 USD Received 16 Nov 2011; revised 23 Dec 2011; accepted 27 Dec 2011; published 19 Jan 2012

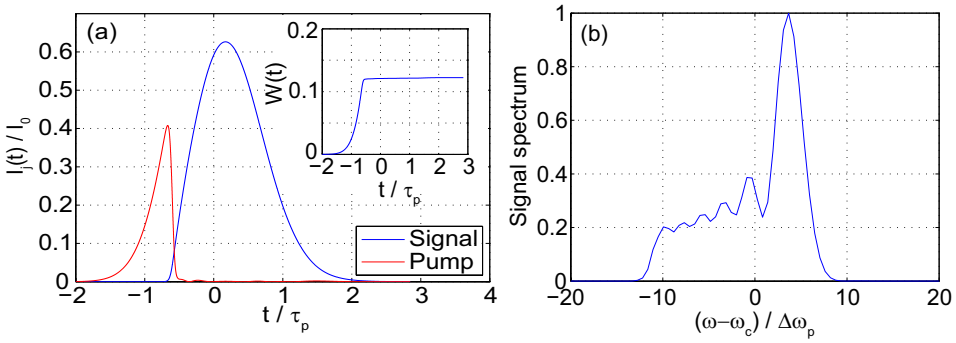

Fig. 4. Output pulses for a chirped QPM OPO with CW-signal-seeding. Simulation parameters are given in the text. (a) Signal and pump intensities $I(t)$ in the time domain, normalized to the peak input pump intensity I_0. The inset shows the normalized output pump fluence $W(t)$, defined in Eq. (17). (b) Signal spectrum, with frequency normalized to the bandwidth of the Gaussian pump pulse ($1/e^2$ duration τ_p) and centered at ω_c, which is defined as the centroid of the signal spectrum.

should satisfy

$$N_{pk} \equiv \frac{2\pi\Lambda_{p,pk}}{\ln(1/R)} \gg 1. \tag{15}$$

Equations (13-15) can be satisfied for any N_{rt} by choosing appropriate values of $\Lambda_{R,pk}$ and R_s, although a more careful analysis is needed for cases when $N_{rt} \not\gg 1$. Assuming $N_{rt} \gg 1$, the next consideration is the signal linewidth. For OPOs with a large N_{pk}, the MI might not be suppressed for cavity modes near the relevant etalon peak (due to the finite etalon finesse), and in this case the signal bandwidth is comparable to the etalon bandwidth. Only one etalon peak should lie within the OPO acceptance bandwidth. This acceptance bandwidth can be approximated as $2\pi\Delta f_{BW} \approx |(\Delta k' L)/(\delta n_g/c)|$, where $\delta n_g = n_g(\omega_s) - n_g(\omega_i)$ for group index $n_g(\omega)$. Thus, the etalon free spectral range f_{fsr} can be constrained according to

$$f_{\mathrm{fsr}} t_{rt} \approx \left| \frac{\Delta k' L^2}{2\pi} \frac{n_g(\omega_s}{\delta n_g} \right|. \tag{16}$$

In order to achieve adiabatic conversion in an apodized chirped grating of the kind described by Eq. (9), it is necessary to have $|\Delta k' L^2| \approx 10^2$, as discussed in Section 3 (although the required grating k-space bandwidth can be reduced slightly by using nonlinear chirp profiles). Hence, in typical cases, the required free spectral range of the etalon satisfies $f_{\mathrm{fsr}} t_{rt} \approx 10^3$. If the minimum etalon length is constrained (e.g. to tens of μm), then Eq. (16) also limits the minimum length of the QPM grating. Therefore, in the following numerical example, we will use a relatively long QPM grating (5 cm) and a pump pulse duration of 15 ns, long enough that $N_{rt} \gg 1$. The final design parameter is the etalon finesse, the effects of which can be explored numerically.

5.2. Numerical example

In this subsection, we show plane-wave numerical examples with a nominal OPO design chosen via the constraints discussed in Subsection 5.1. We assume a 1064-nm-wavelength Gaussian pump pulse with $1/e^2$ duration of 15 ns and a peak intensity of 32 MW/cm^2. The grating length is 5 cm with a chirp rate of 4×10^4 m^{-2} (except in the apodization regions) and a QPM period

#158303 - $15.00 USD Received 16 Nov 2011; revised 23 Dec 2011; accepted 27 Dec 2011; published 19 Jan 2012

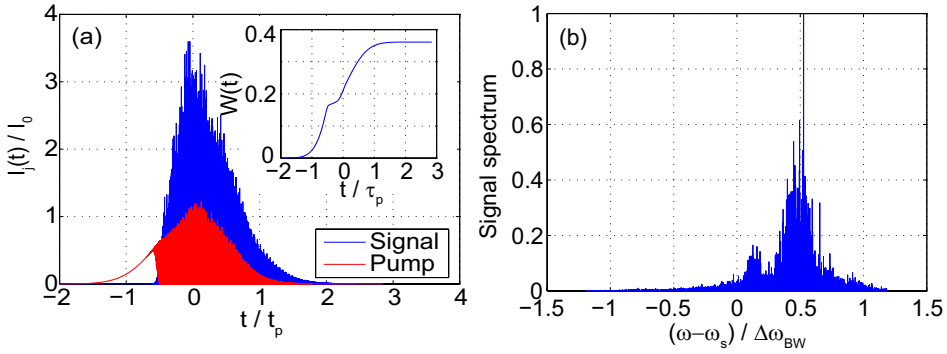

Fig. 5. Output pulses for a chirped QPM OPO with the same parameters as those used in Fig. 4, but with white-noise seeding. (a) Signal and pump intensities in the time domain, $I_j(t)$ ($j = s, p$), normalized to the peak intensity of the input pump pulse, I_0. The inset shows $W(t)$. (b) Signal spectrum, with frequency normalized to the OPO acceptance bandwidth Δf_{BW} (≈ 3.35 THz in this case) and centered at ω_s, the signal frequency phasematched at the center of the QPM grating.

chosen to phasematch a 1550-nm-wavelength signal in the middle of the grating; the grating has a similar profile to the example shown in Fig. 1(b). The round-trip losses were taken to be 19%. With these parameters, $N_{rt} \approx 20.5$, $\Lambda_p \approx 0.95$, and hence the peak times above threshold $N_{pk} \approx 28$. For cases when an intracavity etalon is included, the etalon has a free spectral range of 2 THz and a power reflectance of 64% on each facet. The corresponding etalon bandwidth is $\Delta f_{\text{et}} \approx 120$ GHz, and the product $f_{\text{fsr}} t_{rt} \approx 1450$. The value $|(\Delta k' L^2 n_{g,s})/(2\pi\delta n_g)| \approx 1200$, as discussed in relation to Eq. (16). The simulations use a method similar to the one described in Ref. [20]; the THz wave is neglected.

When the OPO is seeded with a CW signal whose intensity exceeds that of the quantum noise floor, the pump is highly depleted after the initial signal power build-up. This case is shown in Fig. 4, where we assume a signal seed intensity of 1 W/cm^2 and include an intracavity etalon. The pump is highly depleted after the initial signal build-up. The later parts of the pump pulse are also strongly depleted, since the signal-cavity lifetime is comparable to the pump duration. The inset shows the normalized output pump fluence, which we define as

$$W(t) = \frac{\int_{-\infty}^{t} I_p(L,t')dt'}{\int_{-\infty}^{\infty} I_p(0,t')dt'}. \tag{17}$$

After the signal begins to saturate the pump, no further pump energy is transmitted, so the transmitted fluence is limited. This example demonstrates an efficiency enhancement analogous to those predicted by Fig. 1 and Eq. (8), but modified in the presence of a nanosecond Gaussian pump pulse instead of a CW pump. In each pass through the QPM grating, different temporal components of the signal pulse experience adiabatic conversion almost independently, since the pulse bandwidth is much narrower than the bandwidth of any effects related to GVM and GVD. Note that for very high intensities, an intracavity etalon is required in order to suppress the MI even with a CW signal seed, due to the finite bandwidth of the pump; the etalon described above was thus included in the simulations for Fig. 4.

In contrast to the CW case or the pulsed case with a monochromatic seed, in a ns-pumped OPO seeded with white noise the adiabatic conversion process no longer occurs. Since there is a MI at all pump ratios $N > 1$, noise-seeded signal sidebands are amplified over most of the

#158303 - $15.00 USD Received 16 Nov 2011; revised 23 Dec 2011; accepted 27 Dec 2011; published 19 Jan 2012

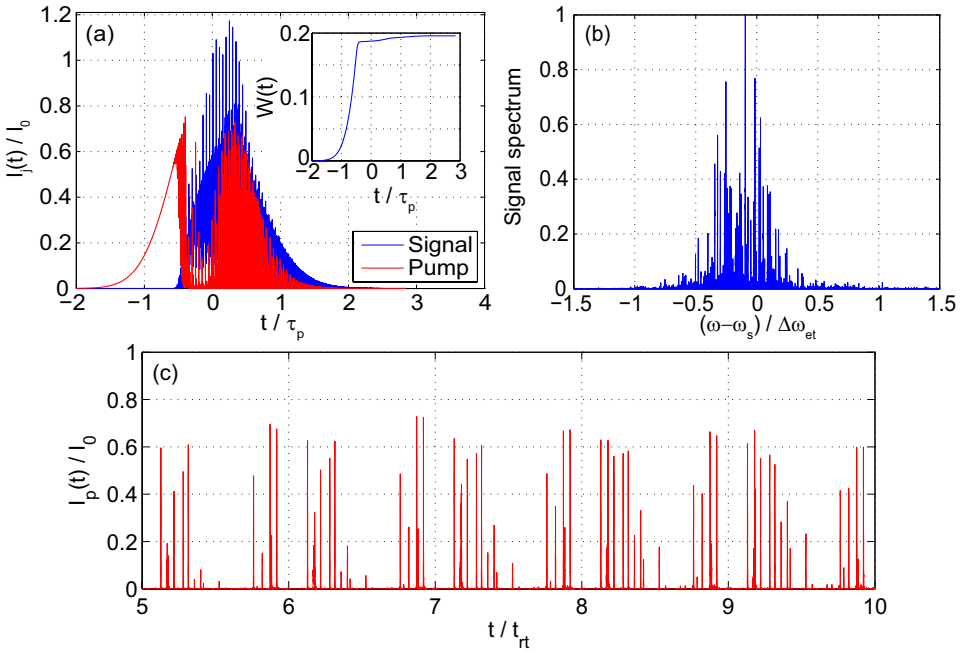

Fig. 6. Output pulses for a chirped QPM OPO with the same parameters as those used in Fig. 5, but with an intracavity etalon (free spectral range 4.15 THz). (a) Signal and pump intensities in the time domain, $I_j(t)$ ($j = s, p$), normalized to I_0. The inset shows $W(t)$. (b) Signal spectrum, with frequency normalized to the bandwidth of the etalon peaks, $\Delta f_{\rm et} = {\rm fsr}_{\rm et}(1-R_{\rm et})/(2\pi)$ for etalon reflectance $R_{\rm et}$ and free spectral range ${\rm fsr}_{\rm et}$. $\Delta f_{\rm et} \approx 120$ GHz in this case. (c) Output pump intensity $I_p(t)/I_0$ for the case shown in Fig. 6(a), plotted over a limited temporal range to show pulsing behavior; the pulses correspond to regions in which adiabatic conversion does not occur. The time axis is normalized to the signal round-trip time: the pulse pattern is slightly modified after each signal round trip through the cavity.

pump pulse. A typical signal spectrum corresponding to a single simulation with a white-noise-seeded signal is shown in Fig. 5(b). The spectrum fills the OPO acceptance bandwidth, which corresponds to several THz. The corresponding transmitted signal and pump intensities $I_j(t)$ are shown in Fig. 5(a). The conversion efficiency associated with this example is significantly reduced compared to Eq. (4) because the smooth signal phase profile required for adiabatic following is no longer present due to seeding with noise rather than a single frequency. This reduction in efficiency can be seen in the inset of Fig. 5(a), which plots $W(t)$.

From the results of Section 4, it is necessary to use an intracavity element such as an etalon to suppress the MI or limit the frequency range over which there is MI gain, and thereby allow adiabatic conversion to occur. This approach is shown in Fig. 6, where an etalon is added to the cavity: this allows the adiabatic conversion efficiency behavior to re-emerge [Fig. 6(a)] even in the presence of a noise seed, by narrowing the signal bandwidth [Fig. 6(b)]. The noise suppression is not complete; the remaining signal noise leads to an output pump which consists of many short pulses which correspond to time intervals in which adiabatic conversion does not occur. The slight reduction in conversion efficiency associated with these output pump pulses can be seen from $W(t)$, which is plotted in the inset of Fig. 6(a): after saturation, the (average) slope $dW(t)/dt$ is positive but small compared to the slope shown in Fig. 5(a). The structure of

#158303 - $15.00 USD Received 16 Nov 2011; revised 23 Dec 2011; accepted 27 Dec 2011; published 19 Jan 2012

the output pump pulses is shown in Fig. 6(c), where $I_p(t)/I_0$ is plotted over a limited temporal region. These output pump spikes correspond to the finite bandwidth of the signal shown in Fig. 6(b), and repeat (approximately) every round-trip time. Conventional nanosecond OPOs can exhibit a similar self-pulsing behavior [20, 23]. Nonetheless, the pump is highly depleted over most of its temporal profile, showing that adiabatic operation of an OPO can be effective even with a noise seed, if a suitable bandwidth-limiting filter is included in the cavity.

The same procedures we have discussed here (identification of an MI and its severity, and calculation of the required etalon properties) could be used at other operating points besides the case simulated in Figs. (4-6). Generally, the etalon finesse required to suppress the MI will scale with N, the suppression of spectral sidebands will scale with this finesse and with N_{rt}, and the MI gain bandwidth (and hence the etalon's required free spectral range) will scale with the OPO signal-idler acceptance bandwidth. If the etalon has a large enough free spectral range that only one etalon peak lies within the OPO acceptance bandwidth but has an insufficient finesse to fully suppress the MI within that peak, the signal bandwidth is comparable to the etalon bandwidth Δf_{et}. To suppress the pump pulsing, a higher finesse etalon could be used; to yield a single- or few-mode signal via intracavity filters with realistic parameters, multiple filters (e.g. a grating and an etalon) or injection seeding might be required.

6. Conclusions

The use of Gaussian beams and unchirped QPM or birefringently phasematched media impose a fundamental limitation to the conversion efficiency of singly-resonant OPOs in the non-diffracting regime due to back-conversion. By using a chirped QPM grating, this limitation could be evaded via the adiabatic conversion process, allowing for a broadly tunable, high-power-spectral-density mid-infrared source. However, the modulation instability we have described in this paper must be suppressed or avoided if such an OPO is to exhibit useful adiabatic pump conversion. One possible approach is to use a CW or narrowband laser as a seed. Another, simpler approach is to use a high-finesse intracavity etalon in order to suppress the unstable spectral sidebands. When operated several times above oscillation threshold with such an etalon, almost all of the pump pulse can be down-converted to the signal and idler waves, even with a Gaussian or other non-flat-top pump pulse profile. The etalon is constrained to have both a relatively high finesse and free spectral range. An alternative approach might be to use multiple intracavity elements to suppress the MI, such as a diffraction grating (to suppress the MI at high sideband frequency detunings) and a longer etalon (to yield a narrow-band signal); with this approach, there would be less stringent design constraints on the etalon.

In this paper we considered the temporal MI of chirped QPM OPOs, but not the spatial MI effects, i.e. the amplification of signal sidebands with non-zero transverse spatial frequency which can also be present, even at temporal frequencies degenerate with the carrier fields [7,36]. A discussion of these effects is beyond the scope of this paper. Spatial MIs can be calculated with the approach discussed in appendix (A) by setting $k_x^2 + k_y^2 > 0$. This type of MI could be suppressed by moderate signal focusing with non-planar cavity mirrors in combination with a spatial filter; for very wide beams, unstable cavity configurations might be used. Spatial MIs and other focusing effects in chirped QPM interactions will be the subject of future work.

The temporal MI we have considered is directly applicable to OPOs which use a narrowband pump. In synchronously pumped OPOs with ps or fs pump pulses with bandwidths comparable to the OPO acceptance bandwidth, the MI would be altered, and may be relevant to explaining the fluctuations observed in Ref. [37]. Finally, the interaction between the effects discussed here and $\chi^{(3)}$ self phase modulation effects could lead to new and interesting types of OPO-based frequency combs.

#158303 - $15.00 USD Received 16 Nov 2011; revised 23 Dec 2011; accepted 27 Dec 2011; published 19 Jan 2012

A. Modulation instability for CW OPO

In this appendix, we develop a formalism for evaluating the MI of the steady-state OPO solutions found in Section 3, based on the coupled wave equations of Section 2. To calculate the MI gain, we follow the approach of Ref. [13]: we assume leading-order fields that are both plane-wave and monochromatic, and find the z-dependent field profiles which satisfy self-consistency in amplitude and phase after a single cavity round-trip. We then assume weak time-dependent perturbations around these zeroth-order solutions and solve the linear system which results from neglecting products of the perturbations, or sidebands, a_j. The envelopes are assumed to have the form

$$A_j(\mathbf{r},t) = A_j^{(0)}(z) + a_j(\mathbf{r},t) \tag{18}$$

for zeroth-order fields $A_j^{(0)}(z)$ and perturbations $a_j(\mathbf{r},t)$. The zeroth-order fields $A_j^{(0)}$ have optical frequencies ω_j and have spatial frequencies $k_x = k_y = 0$.

For a particular input pump field and vanishing idler input, amplitude self-consistency of the zeroth-order fields requires that $|A_s^{(0)}(L)|R_s^{1/2} = |A_s^{(0)}(0)|$ for net round-trip signal-power reflectance R_s; this relation determines $|A_s^{(0)}(0)|$ as a function of $|A_p^{(0)}(0)|$, and hence as a function of the pump ratio N, for a given system. We assume that the signal carrier frequency corresponds to an axial mode of the cavity [15, 38]. Therefore, the cavity adds an additional phase such that the phase of the electric field, $\tilde{E}_s(\omega_s)$, is also self-consistent after a cavity round-trip. Although $A_j^{(0)}$ are found numerically via Eq. (1), the simple relations in Section 3 provide useful estimates of how these fields behave.

To describe how the sideband amplitudes a_j are coupled to each other in the presence of the zeroth-order fields, we define spatial frequency vector $\mathbf{k}_\perp = k_x\hat{\mathbf{x}} + k_y\hat{\mathbf{y}}$ and sideband frequency $\Omega = |\omega - \omega_j|$. Because we assume $k_x = k_y = 0$ for $A_j^{(0)}$, the a_j can only be coupled together in a limited number of ways. To write down the coupling matrix, we first introduce a shorthand notation for the sidebands: $a_j(z;\mathbf{k}_\perp,\Omega) \equiv a_j^{(+)}$ and $a_j(z;-\mathbf{k}_\perp,-\Omega) \equiv a_j^{(-)}$. The sideband frequency $\Omega \geq 0$, while k_x and k_y can be positive or negative. We now define a sideband vector

$$\tilde{v}(\mathbf{k}_\perp,\Omega)^T \equiv \left[\tilde{a}_i^{(-)*} \quad \tilde{a}_i^{(+)} \quad \tilde{a}_s^{(-)*} \quad \tilde{a}_s^{(+)} \quad \tilde{a}_p^{(-)*} \quad \tilde{a}_p^{(+)} \quad \tilde{a}_T^{(+)}\right], \tag{19}$$

where the dependencies of $\tilde{a}_j^{(\pm)}$ on z, $\mathbf{k}_\perp$, and Ω have been suppressed. For the DC envelope, only $\tilde{a}_T^+$ is included in Eq. (19), due to the use of analytic signals for each of the envelopes; as such, it is implicitly assumed that $\Omega < \omega_j$ for $j = (i,s,p)$ (an appropriate assumption when the OPO acceptance bandwidth is much less than the pump, signal and idler carrier frequencies, which is almost always the case). Propagation for this sideband vector is described by a linear system,

$$\frac{d\tilde{v}}{dz} = M(z)\tilde{v} \tag{20}$$

where $M(z)$ is a 7x7 coupling matrix which depends on the frequency-domain arguments as well as z. Due to the assumed axial symmetry of the problem, the same coupling matrix applies to both $\tilde{v}(+\mathbf{k}_\perp,\Omega)$ and $\tilde{v}(-\mathbf{k}_\perp,\Omega)$ for arbitrary $\mathbf{k}_\perp$. The coupling matrix $M(z)$ has a form similar to the one introduced in Ref. [13], but with extra elements for the THz sideband a_T^+ associated

#158303 - $15.00 USD Received 16 Nov 2011; revised 23 Dec 2011; accepted 27 Dec 2011; published 19 Jan 2012

with the DC envelope $\tilde{A}_T$ in Eq. (1),

$$\mathbf{M}(z) = i\begin{bmatrix} -K_{i,-} & 0 & 0 & \kappa_{i,\mathrm{o}}^{-}A_p^{(0)*} & \kappa_{i,\mathrm{o}}^{-}A_s^{(0)} & 0 & \kappa_{i,\mathrm{T}}^{-}A_i^{(0)*} \\ 0 & -K_{i,+} & -\kappa_{i,\mathrm{o}}^{+}A_p^{(0)} & 0 & 0 & -\kappa_{i,\mathrm{o}}^{+}A_s^{(0)*} & -\kappa_{i,\mathrm{T}}^{+}A_i^{(0)} \\ 0 & \kappa_{s,\mathrm{o}}^{-}A_p^{(0)*} & -K_{s,-} & 0 & \kappa_{s,\mathrm{o}}^{-}A_i^{(0)} & 0 & \kappa_{s,\mathrm{T}}^{-}A_s^{(0)*} \\ -\kappa_{s,\mathrm{o}}^{+}A_p^{(0)} & 0 & 0 & -K_{s,+} & 0 & -\kappa_{s,\mathrm{o}}^{+}A_i^{(0)*} & -\kappa_{s,\mathrm{T}}^{-}A_s^{(0)} \\ \kappa_{p,\mathrm{o}}^{-}A_s^{(0)*} & 0 & \kappa_{p,\mathrm{o}}^{-}A_i^{(0)*} & 0 & -K_{p,-} & 0 & \kappa_{p,\mathrm{T}}^{-}A_p^{(0)*} \\ 0 & -\kappa_{p,\mathrm{o}}^{+}A_s^{(0)} & 0 & -\kappa_{p,\mathrm{o}}^{+}A_i^{(0)} & 0 & -K_{p,+} & -\kappa_{p,\mathrm{T}}^{+}A_p^{(0)} \\ \kappa_T A_i^{(0)} & \kappa_T A_i^{(0)*} & \kappa_T A_s^{(0)} & \kappa_T A_s^{(0)*} & \kappa_T A_p^{(0)} & \kappa_T A_p^{(0)*} & -K_{T,+} \end{bmatrix} \tag{21}$$

where the elements of this matrix are defined in terms of the operators and coefficients of Eq. (1), with $\kappa_{j,\mathrm{o}}^{\pm} = \gamma_{\mathrm{opt}}(\omega_j \pm \Omega)$, $\kappa_{j,\mathrm{T}}^{\pm} = \gamma_{\mathrm{THz}}(\omega_j \pm \Omega)$, $\kappa_T = \gamma_{\mathrm{THz}}(\Omega)$, $K_{j,\pm}(z,\Omega) = \pm[k(\omega_j \pm \Omega) - k(\omega_j) - (k_x^2 + k_y^2)/(2k(\omega_j \pm \Omega)] - \Omega/v_{\mathrm{ref}} \mp \Delta k(z)$, and $K_{T,+} = i\alpha_T/2 - \left[k(\Omega) - (k_x^2+k_y^2)/(2k(\Omega)) + \Omega/v_{\mathrm{ref}} - K_g\right]$. The diagonal elements of M are determined by the linear differential operators $\hat{L}_j$ [Eqs. (4) and (5)], while the off-diagonal elements determine coupling between the sideband vectors due to $\chi^{(2)}$ interactions. For chirped QPM gratings, all the non-zero elements of M are z-dependent.

The last step in calculating the MI is to calculate a total round-trip matrix which propagates the sideband vector $\tilde{v}$ through a full cavity round-trip. For the MI of a singly-resonant OPO where the idler and pump fields and their sidebands have zero feedback, only the 2x2 submatrix related to the signal, denoted $\tilde{v}_s$, must be considered. The phase and amplitude response of the cavity at frequency ω_s are fixed by self-consistency (in a real OPO, self-consistency would determine ω_s; for this theoretical study, it is convenient to fix ω_s and slightly adjust the cavity length accordingly). Therefore, the round-trip signal-sideband matrix is given by

$$\Phi_{rt}(\Omega) = \sqrt{R_s}\begin{bmatrix} \tilde{h}^*(-\Omega)e^{i\phi_s} & 0 \\ 0 & \tilde{h}(\Omega)e^{-i\phi_s} \end{bmatrix}\begin{bmatrix} \Phi_{3,3}(L,0) & \Phi_{3,4}(L,0) \\ \Phi_{4,3}(L,0) & \Phi_{4,4}(L,0) \end{bmatrix}, \tag{22}$$

where the state transition matrix Φ is defined using $M(z)$ and Eq. (20) as $\tilde{v}(z') = \Phi(z',z)\tilde{v}(z)$. The 2x2 submatrix of $\Phi(L,0)$ appearing in Eq. (22) corresponds to the outputs at the signal sideband frequencies resulting from inputs at those frequencies. The output phase of the zeroth-order signal, $A_s^{(0)}(L)/A_s^{(0)}(0)$, is defined as ϕ_s. To account for intracavity elements a normalized cavity transfer function $\tilde{h}(\Omega) = \tilde{H}(\Omega)/\tilde{H}(0)$ has been introduced in terms of the transfer function $\tilde{H}(\Omega)$ associated with the cavity excluding the QPM grating; $\tilde{h}$ would include any intracavity etalon, for example. Note that since the THz wave propagates backwards, its absorption appears mathematically as a "gain" in Eqs. (20) and (21). As a result, it is useful numerically to first solve Eq. (20) by propagating backwards (finding a matrix giving $\tilde{v}(z=0)$ in terms of $\tilde{v}(z=L)$), and then find Φ by matrix inversion.

There are two eigenvalues of Φ_{rt}, denoted $\lambda_{\Phi,j}$ for $j=1$ and $j=2$. Modes of the "hot" cavity are those frequencies for which $\lambda_{\Phi,j}$ are real; these frequencies can differ from the frequencies of the "cold" cavity modes as a result of phase shifts due to the three-wave interaction, and due to coupling between frequencies at $+\Omega$ and $-\Omega$. Exponential growth (MI) of such a cavity mode occurs when $\lambda_{\Phi,j}(\Omega) > 1$, for some j and some Ω. We assume that the cavity modes are closely-spaced in frequency compared to the variation of the eigenvalues with sideband frequency Ω; therefore, we can define the MI condition as $|\lambda_{\Phi,j}| > 1$. A more detailed description of the MI calculation is given in Ref. [13].

#158303 - $15.00 USD Received 16 Nov 2011; revised 23 Dec 2011; accepted 27 Dec 2011; published 19 Jan 2012

Acknowledgments

This research was supported by the U.S. Air Force Office of Scientific Research (AFOSR) under grants FA9550-09-1-0233 and FA9550-05-1-0180.

#158303 - $15.00 USD Received 16 Nov 2011; revised 23 Dec 2011; accepted 27 Dec 2011; published 19 Jan 2012